

Article

New Insights on the Understanding of Sulfur-Containing Coal Flotation Desulfurization

Gan Cheng ^{1,2,*}, Yulong Li ³, Yijun Cao ⁴, Xin Wang ¹, Enze Li ^{1,2}, Yanxia Guo ^{1,2} and Ee Von Lau ⁵¹ Institute of Resources and Environmental Engineering, Shanxi University, Taiyuan 030031, China² Shanxi Laboratory for Yellow River, Shanxi University, Taiyuan 030031, China³ College of Chemistry and Chemical Engineering, Henan Polytechnic University, Jiaozuo 454003, China⁴ School of Chemical Engineering, Zhengzhou University, Zhengzhou 450001, China⁵ School of Engineering, Monash University Malaysia, Selangor 47500, Malaysia; lau.ee.von@monash.edu

* Correspondence: chenggan464@126.com

Abstract: The clean and efficient utilization of coal is a promising way to achieve carbon neutrality. Coking coal is a scarce resource and an important raw material in the steel industry. However, the presence of pyrite sulfur affects its clean utilization. Nonetheless, this pyrite could be removed using depressants during flotation. Commonly used organic depressants (sodium lignosulfonate (SL), calcium lignosulfonate (CL), and pyrogallol (PY)) and inorganic depressants (calcium oxide (CaO) and calcium hypochlorite (Ca(ClO)₂)) were chosen in this study. Their inhibition mechanism was discussed using FTIR, XPS, and molecular dynamics (MD) methods. The desulfurization ability of organic depressants was shown to be better than inorganic ones. Among the organic depressants, PY proved to be advantageous in terms of low dosage. Physical adsorption was identified as the main interaction form of SL, CL, and PY onto the surface of pyrite, as evidenced from FTIR and XPS analyses. Similarly, MD simulation results showed that hydrogen bonds played a proactive role in the interactions between PY and pyrite. The diffusion coefficient of water molecules on the pyrite surface was also observed to decrease when organic depressants were present, indicating an increase in the hydrophilicity of pyrite. This research is of great significance to utilize sulfur-containing coal and minerals.

Keywords: coal flotation; desulfurization; pyrite; sulfur

Citation: Cheng, G.; Li, Y.; Cao, Y.; Wang, X.; Li, E.; Guo, Y.; Lau, E.V. New Insights on the Understanding of Sulfur-Containing Coal Flotation Desulfurization. *Minerals* **2024**, *14*, 981. <https://doi.org/10.3390/min14100981>

Academic Editor: William Skinner

Received: 12 August 2024

Revised: 26 September 2024

Accepted: 27 September 2024

Published: 29 September 2024



Copyright: © 2024 by the authors. Licensee MDPI, Basel, Switzerland. This article is an open access article distributed under the terms and conditions of the Creative Commons Attribution (CC BY) license (<https://creativecommons.org/licenses/by/4.0/>).

1. Introduction

Coal is one of the most abundant and cost-effective energy resources in the world, and accounts for 37% of the world's electricity [1,2]. In 2020 alone, the world's proven coal reserves stood at 1.07 trillion tons [3]. According to the *World Energy & Climate Statistics—Yearbook 2021* [4], the world's top five coal producers in 2020 were China, India, Indonesia, the United States, and Australia, with a total coal production of 3743 Mt, 779 Mt, 551 Mt, 488 Mt, and 473 Mt, respectively. As the largest coal producing country (49% of the global output), the coal production in China was said to grow by 1.4%. According to the country's National Bureau of Statistics, China's raw coal production increased by 4.7% to 4.07 Gt while imports grew by 6.6% to 323 Mt in the year 2021. At present, environmental pollution is one of the main factors influencing the exploitation and utilization of coal resources [5,6]. In China, about 80% of coal is used as fuel [7], in which gaseous sulfur dioxide (SO₂) is released during coal combustion, causing environmental and health concerns. Unfortunately, about 1/3 of the total coal reserves in China are attributed to high-sulfur coal [8]. Thus, there is a need to reduce the sulfur content in coal not only to reduce the emission of SO₂ in the process of coal burning, but also help to fully utilize China's coking coal resources while improving the quality of steel produced [9], which is of great significance to the rational utilization of these coal resources [10].

The World Steel Association forecast global finished steel consumption to increase by 1.8% in 2023 and increase by 1.9% in 2024. The final steel products originate from iron ore. As shown in Figure 1, the global iron ore reserves and the proportion of available iron ore for 2023 are presented. Among iron ore deposits, pyrite (FeS_2) accounts for the largest proportion. Pyrite is a significant sulfide mineral resource, rich in both iron and sulfur. Researching and evaluating the separation of pyrite is crucial for flotation, mineral processing, and smelting.

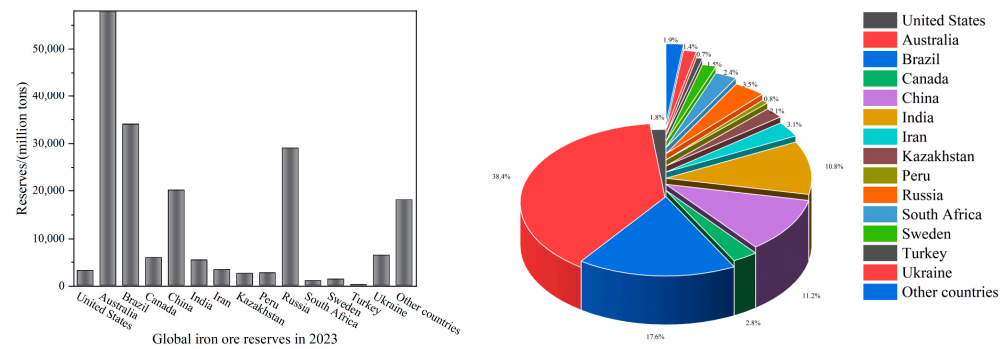
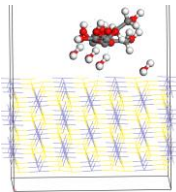
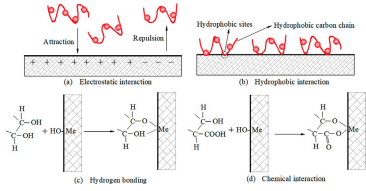
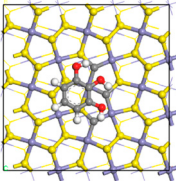
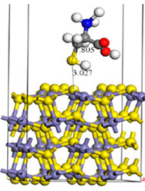
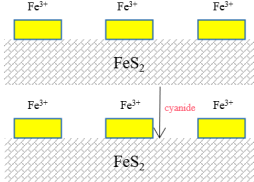
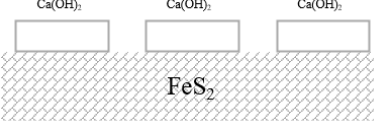
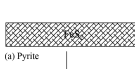
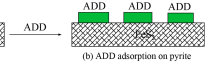
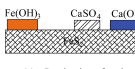
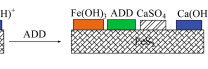


Figure 1. Iron ore reserves and proportion of available iron ore.

Flotation is commonly employed as one of the effective physical methods to remove inorganic sulfur in fine coal. During flotation, the lattice defects of pyrite lead to a difference in hydrophilicity [11]. Ahmad et al. [12] removed 49.83% of total sulfur and 43.79% of ash from low-rank coal using Triton X-100 as the frother (400 ppm) and diesel oil as the collector (0.2 mL). Figure 2 shows the lattice defects of pyrite in different ores. For pure pyrite, pyrite forms a surface facial mask after absorbing oxygen in the air; for ore pyrite, pyrite is activated by Cu^{2+} and Pb^{2+} in the flotation pulp; for coal pyrite, coal and pyrite form a symbiosis and pyrite forms hydrophobic products after oxidation. The coal seams are usually formed in swamps or shallow water bodies; these environments are rich in organic matter and lack oxygen, often containing a certain amount of sulfur. The surrounding geological layers contain iron minerals or dissolved iron ions that interact with sulfides to form pyrite, which crystallizes and precipitates in the pores of the coal, thus forming in the coal seam together with organic matter. During the mineralization process of pyrite, the loss of cations or anions leads to vacancy defects, while some impurity atoms are doped into the interior of the pyrite lattice, affecting the oxidation of the mineral surface. Vacancy defects, doped atoms, and surface oxidation can all cause changes in electronic structural properties, which in turn affect the surface hydrophobicity. These reasons explain why pyrite is difficult to depress [13,14]. Depressants can be used to selectively adsorb and improve the hydrophilicity of pyrite [15,16], thus providing a conducive environment to the separation of coal and pyrite [17]. There are organic and inorganic depressants for pyrite. Starch, polysaccharide, lignosulfonate, pyrogallol, mercaptoacetic acid, etc. are common organic depressants, while inorganic depressants include cyanide, lime, calcium hypochlorite, etc. Table 1 shows the mechanism of organic and inorganic depressants in pyrite flotation. Pyrite is inhibited from flotation by starch through the formation of hydrogen bonds between polar group molecules. Fe^{2+} and ferrous oxide are oxidized by lignosulfonate to form hydrophilic material ferric oxide, which inhibits the flotation of pyrite. Pyrite is inhibited from flotation by iron series complexes formed by pyrogallol and pyrite [18]. Thioglycolic acid ($-\text{SH}$) is adsorbed on pyrite to increase its surface electronegativity and inhibit pyrite flotation. The adsorption of the collector is inhibited by the formation of ferrocyanide from cyanide and pyrite [19]. Pyrite is inhibited by the hydrophilic material $\text{Ca}(\text{OH})_2$ adsorbed on the surface. Pyrite is oxidized by calcium hypochlorite to precipitate and inhibit the adsorption of collectors [20]. Liu and Wu [21] noted that thioglycolic acid has a stronger inhibition ability on pyrite than vitamin C and calcium oxide. Liu et al. [22] compared the inhibition ability of konjac glucomannan, guar gum, and dextrin at a dosage of 10 mg/L,

in which the recovery of pyrite was found to be 2.11%, 27.46%, and 33.68%, respectively. Zhou et al. [23] floated pyrite selectively from sub-bituminous and meta-bituminous coal using potassium amyl xanthate as the collector and starch as the depressant. The flotation recoveries of pyrite were over 95%, with a pyrite grade of over 95% in the concentrates.

Table 1. Mechanism of organic and inorganic depressants in pyrite flotation.

Classification	Name	Mechanization	Mechanism Diagram	
Organic depressants	Starch, Polysaccharide	The formation of hydrogen bonds between polar groups molecules (such as hydroxyl and carboxyl groups) inhibits pyrite flotation.		
	Lignosulfonate	Oxidizes Fe ²⁺ and FeO into hydrophilic material Fe ₂ O ₃ and inhibits the pyrite flotation.		
	Pyrogallol	Pyrogallol and pyrite form iron series complex to inhibit pyrite flotation.		
	Mercaptoacetic acid	Adsorption of mercaptoacetic (-SH) on the surface of pyrite to improve its surface electronegativity and inhibit pyrite flotation.		
Inorganic depressants	Cyanide	The formation of ferricyanide on the surface of pyrite inhibits the adsorption of collectors.		
	Lime	Adsorption of hydrophilic material Ca(OH) ₂ on the pyrite surface inhibits pyrite flotation.		
	Calcium hypochlorite		FeS ₂ is oxidized by Ca(ClO) ₂ into Fe(OH) ₃ precipitate and inhibits the collector adsorption.	
				  

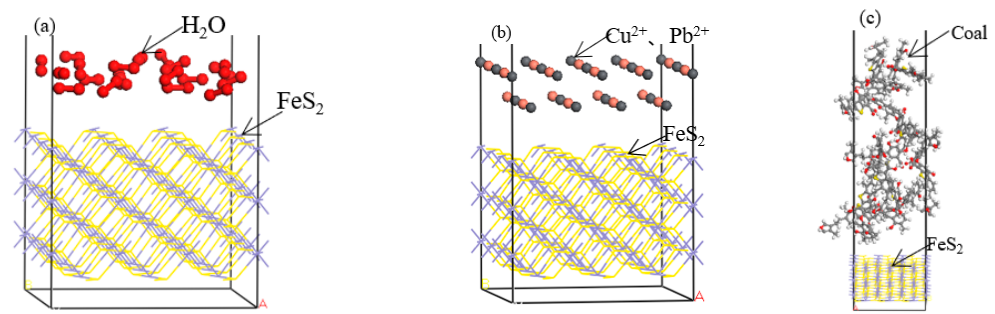


Figure 2. Diagram of different pyrite: (a) pure pyrite; (b) ore pyrite; (c) coal pyrite.

The study of the adsorption mechanism between depressants and pyrite is helpful to the development of new reagents [24]. In addition to XPS, FTIR, and other analytical techniques, MD simulation is an effective tool to study the interfacial interaction between reagents and the mineral surface at the atomic scale [25]. Chen et al. [26] found that the adsorption energy between xanthate ions and pyrite was -233.35 kJ/mol under anaerobic conditions; this dropped to -215.19 kJ/mol when oxygen was presented, indicating that O_2 is not conducive to the adsorption of xanthate ions on pyrite. Zheng et al. [27] compared the adsorption configurations of four groups (-SH, $-NH_3$, =O, and -O) of cysteine on pyrite. Their results showed that the adsorption stability of these four groups of cysteine on the Fe site was stronger than that of the S site, while the O-Fe bond length was the shortest (2.155 Å) compared with -S-S, -S-Fe, -N-S, -N-Fe, =O-S, =O-Fe, and -O-S, indicating that the adsorption of -O on the Fe site of pyrite was the most stable. Xia et al. [28] simulated the adsorption of dodecyltrimethylammonium bromide (DTAB) on the surface of low-rank coal and observed that DTAB molecules were adsorbed onto the low-rank coal surface mainly by electrostatic force. In addition, the nitrogen atom in the DTAB molecule appears as the active site, while the alkyl group oriented towards the water phase, thus inhibiting the adsorption of water molecule onto the coal surface. Guo et al. [29] simulated the adsorption of the non-ionic surfactants n-dodecyl β -D-maltoside ($C_{12}G_2$) and dodecyl hepta glycol ($C_{12}E_7$) on the surface of lignite. The adsorption of $C_{12}G_2$ and $C_{12}E_7$ was via a physical interaction. In addition, some researchers suggested that the electrostatic repulsion between macromolecule depressants and pyrite could be reduced by the hydrolyzed products of Ca^{2+} ($Ca(OH)^+$, $Ca(OH)_2$), which is conducive to the adsorption of macromolecule depressants on the pyrite surface. A review of numerous studies on pyrite adsorption and inhibitors has revealed that, in pyrite systems, multiple influencing factors exist, and the reaction mechanisms are not yet fully understood, making the adsorption mechanism complex and challenging to decipher.

In this work, pyrite was depressed using organic depressants (sodium lignosulphonate (SL), calcium lignosulphonate (CL), and pyrogallol (PY)) and inorganic depressants (calcium oxide (CO) and calcium hypochlorite (CH)), and their inhibition ability as well as flotation performances were compared. In addition, the inhibition mechanism of depressants and pyrite was also discussed using FTIR, XPS analysis, and MD simulation methods.

2. Experimental

2.1. Materials and Chemicals

Sulfur-containing coal sample was obtained from Henan Province, China. The coal sample was crushed and ground to approximately 0.5 mm particle size in a rod mill. For surface analyses, including adsorption capacity, FTIR spectral analysis and XPS spectroscopy, the coal pyrite sample was further crushed and ground to approximately 0.074 mm. All ground samples were preserved under sealed conditions to prevent oxidation. Flotation reagents including analytical collector (Diethyl phthalate), SL, CL, PY, CO, and CH were purchased from Shanghai Macklin Biochemical Co., Ltd., Shanghai, China. The analytical frother (Octanol) was received from Tianjin Kemiou Chemical Reagent Co., Ltd., Tianjin, China.

2.2. Flotation Experiments

An XFD-V 1 L flotation machine was used to conduct flotation experiments. During the experiment, the pulp was prepared by dispersing 60 g of ground coal and a defined amount of depressant into the plexiglass cell containing 1 L of water. The pulp was then stirred for 2 min at an impeller speed of 1800 rpm. The desired collector and frother were then added independently into the flotation cell and stirred for 1 min and 10 s, respectively. The dosages of collector and frother were both $120 \text{ g}\cdot\text{t}^{-1}$, and the aeration volume was 200 L/h. Finally, froth flotation was carried out for 5 min. The ash content of the product was measured using muffle furnace, and the sulfur content was measured using an automated sulfur analyzer.

2.3. Adsorption Analysis

The total organic carbon analyzer (vario TOC, Elementar Analysensysteme GmbH, Langensfeld, Germany) was used to measure the amount of depressants adsorbed on coal-pyrite. The process was as follows: 2 g of 0.074 mm coal-pyrite was added into 40 mL of depressant solution and the pH value was adjusted to 7.0 using HCl or NaOH solution. The solution was stirred for 10 min under closed condition, and then filtered. The remaining times were recorded, with the average value taken as the final result. All experiments were carried out at room temperature ($25 \pm 3 \text{ C}$). The amount of adsorption was calculated as follows [30]:

$$\Gamma = \frac{V}{M}(C_0 - C) \quad (1)$$

where Γ represents the adsorbed amount (mg/g), V is the volume of the solution (L), C_0 and C are the concentrations of depressants in the initial solution and supernatant, respectively (mg/L), and m represents the mass of the mineral sample (g).

2.4. FTIR and XPS

FTIR spectral analysis was performed using a Perkin Elmer Frontier FTIR spectrometer (PerkinElmer Frontier, Shelton, CT, USA) in the range of $4000\text{--}400 \text{ cm}^{-1}$. The sample preparation method was as follows: 2 g coal-pyrite with a particle size of $\sim 0.074 \text{ mm}$ was added into 50 mL of depressant solution (100 mg/L). Magnetic stirring was then carried out for 30 min at room temperature, and the product was filtered. The filtered product was then dried in a vacuum drying oven for 24 hours at $60 \text{ }^\circ\text{C}$, prior to subjecting the sample to FTIR analysis. X-ray photoelectron spectrometer (ESCALAB 250Xi, ThermoFischer Scientific, Waltham, MA, USA) with Al K α as the sputtering source ($h\nu=1486.6 \text{ eV}$) at 12.5 kV and 16 mA was used. The test pass energy was 50 eV for the full spectrum and 20 eV for the narrow spectrum, the step size was 0.05 eV, the residence time was 40–50 ms, and the binding energy C 1s=284.80 eV was used as the energy standard for charge correction. Peak fitting and quantitative analysis of the spectra were performed using Avantage 5.9918 software. The sample preparation procedure was the same as with FTIR analysis. XRD spectral analysis was performed using an X'Pert3 Powder XRD (Panaco, Almelo, Netherlands). We ground the coal sample to ~ 325 mesh to meet the instrument testing requirements. After the test was completed, the XRD pattern was analyzed using MDI Jade 6.0 software (Materials Data Inc., Livermore, CA, USA) to obtain mineral information of the coal sample. SEM-EDS analysis was performed using a ZEISS Gemini 300 SEM-EDS (Zeiss, Oberkochen, Germany). We performed energy spectrum analysis on coal samples in a certain area at a magnification of 200 times.

2.5. MD Simulation

Materials Studio 2019 simulation software was used in this work. The single crystal cell of pyrite is shown in Figure 3a. Adsorption studies were performed using surface supercell that corresponded to (3×3) pyrite surface unit cells. CASTEP module (CASTEP Developers' Group, Cambridge, UK) was used to optimize the crystal model of pyrite. Dmol³ module was used to optimize the structure of depressant molecules. The optimal

configuration of PY and lignosulfonate (LS) are shown in Figure 3b,c, respectively. The coal molecular model was adapted from Wiser bituminous coal model (Figure 3d), and the molecular formula is $C_{37}H_{32}O_7S$. The optimized depressant molecule was placed in a $30 \text{ \AA} \times 30 \text{ \AA} \times 30 \text{ \AA}$ cubic cell for optimization and energy calculation. CASTEP module was used to optimize the adsorption configuration of depressants on pyrite surface. GGA-PBE was selected as the functional, DNP as the basis group, OTFG ultrasoft as the pseudopotentiality, and DFT-D dispersion was used in the calculation. The calculation accuracy was also set to fine [31]. The simulation process of stable adsorption configuration of depressant on the pyrite surface is shown in Figure 3e.

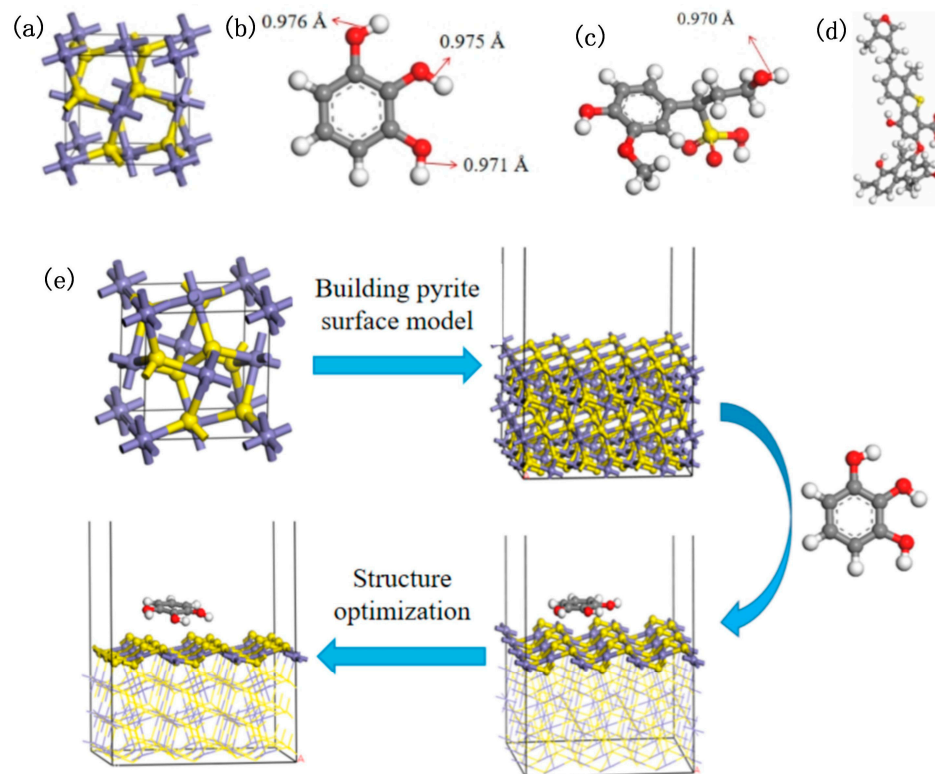


Figure 3. The model of (a) pyrite, (b) PY, (c) LS, (d) coal molecule, and (e) the simulation process of stable adsorption configuration of depressant on the pyrite surface.

Based on the difference between the potential energy of the adsorption complex, the adsorption energy was calculated as follows:

$$E_{\text{ads}} = E_{\text{t}} - E_{\text{d}} - E_{\text{p}} \quad (2)$$

where E_{ads} denotes the adsorption energy between depressants and pyrite, E_{t} denotes the total energy of the adsorption system, E_{d} denotes the energy of depressant, and E_{p} denotes the energy of pyrite. A high negative value of the interaction energy indicates a more favorable interaction.

The dynamic behavior of water molecules on the pyrite surface was influenced by depressant. To determine the effects of depressant on the aggregation features of water molecules, the diffusion coefficients (D) were determined as follows:

$$MSD = \frac{1}{N} \sum_{i=1}^N [r_i(t) - r_i(0)]^2 \quad (3)$$

$$D = \frac{1}{6N} \lim_{t \rightarrow \infty} \frac{d}{dt} \sum_{i=1}^N [r_i(t) - r_i(0)]^2 \quad (4)$$

$$D = \lim_{t \rightarrow \infty} \left(\frac{MSD}{6t} \right) = \frac{1}{6} K_{MSD} \tag{5}$$

where MSD denotes the mean square displacement, N denotes the number of diffusion molecules, $r(t)$ and $r(0)$ denote the position vector of a molecule at time t and $t = 0$, respectively, and K_{MSD} denotes the slope of the MSD curve.

In this study, to investigate the influence of depressant on the dynamics behavior of water molecules on pyrite surface, a depressant molecule and 200 water molecules were placed above the pyrite surface, and another system of water molecules on pyrite surface was included for comparison. At the top of each system, a vacuum slab with a thickness of 50 Å was included to eliminate the periodic boundary conditions in the Z direction. Universal forcefield was adopted for the MD simulation. The constant particle number, volume, and temperature (NVT) ensemble and the Nosé thermostat were selected. The Ewald summation method was used to calculate the long-range electrostatic interaction, while the atom-based method was used to calculate the van der Waals interaction. The total simulation time was 1 ns.

3. Results and Discussion

3.1. The Analyses of Coal Sample

The proximate and ultimate analyses of the coal sample are shown in Figure 4a,b. It can be seen that the moisture content in the coal sample was 1.20% and the ash content was 46.16%, belonging to the ultra-high-ash coal; the volatile content was 15.01%, belonging to the high-volatile coal; the fixed carbon and carbon content were 37.63% and 46.17%, respectively, and the sulfur content was 2.55%, belonging to the medium-high-sulfur coal. The pyritic sulfur content was 1.42% in coal, followed by an organic sulfur content of 0.96%, and a sulfate sulfur content of 0.17%.

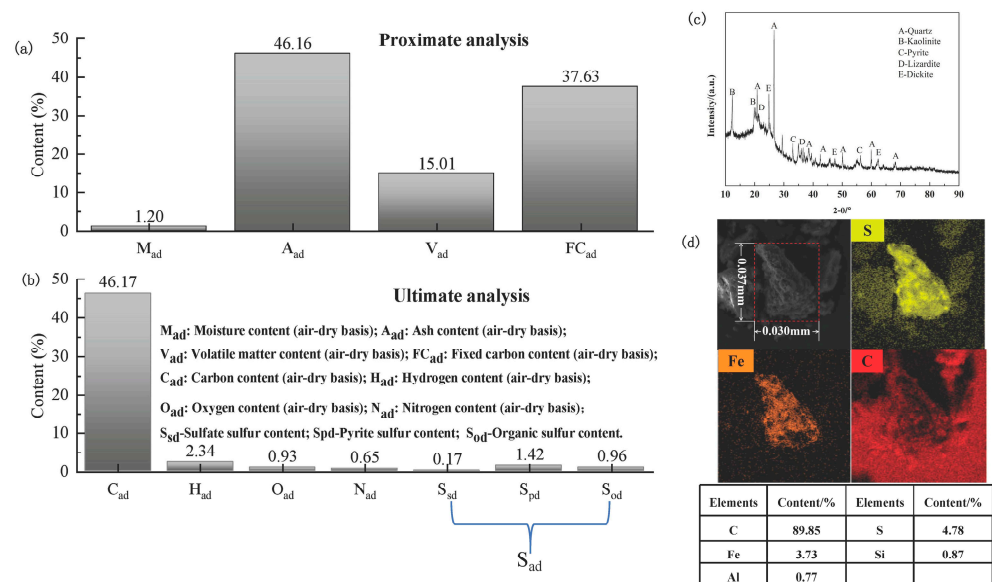


Figure 4. The analysis results of coal sample: (a) proximate analysis, (b) ultimate analysis, (c) X-ray diffraction patterns, and (d) SEM-EDS images.

The XRD result is shown in Figure 4c. Minerals including quartz, kaolinite, pyrite, serpentine, etc. were identified in the coal sample, in which quartz was the dominant mineral component. Compared to quartz, clay minerals (such as kaolinite) were prone to sludge in water and entered into the clean coal through foam entrainment during the flotation, affecting the quality of clean coal.

The SEM-EDS images of the coal sample used in this study are shown in Figure 4d. It can be observed that the element content of S and Fe were 4.78% and 3.73%, respectively,

and the element content ratio S/Fe was 1.28%, which is close to the pyrite (FeS_2) element ratio of 1.14%, and the signal overlap area of S and Fe elements was obvious, indicating that the particle in the picture is pyrite. In addition, an obvious C element signal appeared on the pyrite surface, indicating that there was C atom doping on the pyrite surface.

3.2. Flotation Results

As depicted in Figure 5a–e, as the dosage of organic depressants (SL, CL, PY) increased, the sulfur content, ash content, yield, and combustible recovery of the clean coal decreased gradually. Additionally, the sulfur content of the clean coal was also observed to decrease from 2.55% to below 1.60%, while the flotation of clean coal was found to be inhibited by organic depressants. On the other hand, the sulfur content, ash content, yield, and combustible recovery in clean coal showed no obvious changes with an increase in inorganic inhibitors (CO, CH). While the sulfur content was observed to remain above 1.80%, evidence of poor desulfurization performance was also witnessed.

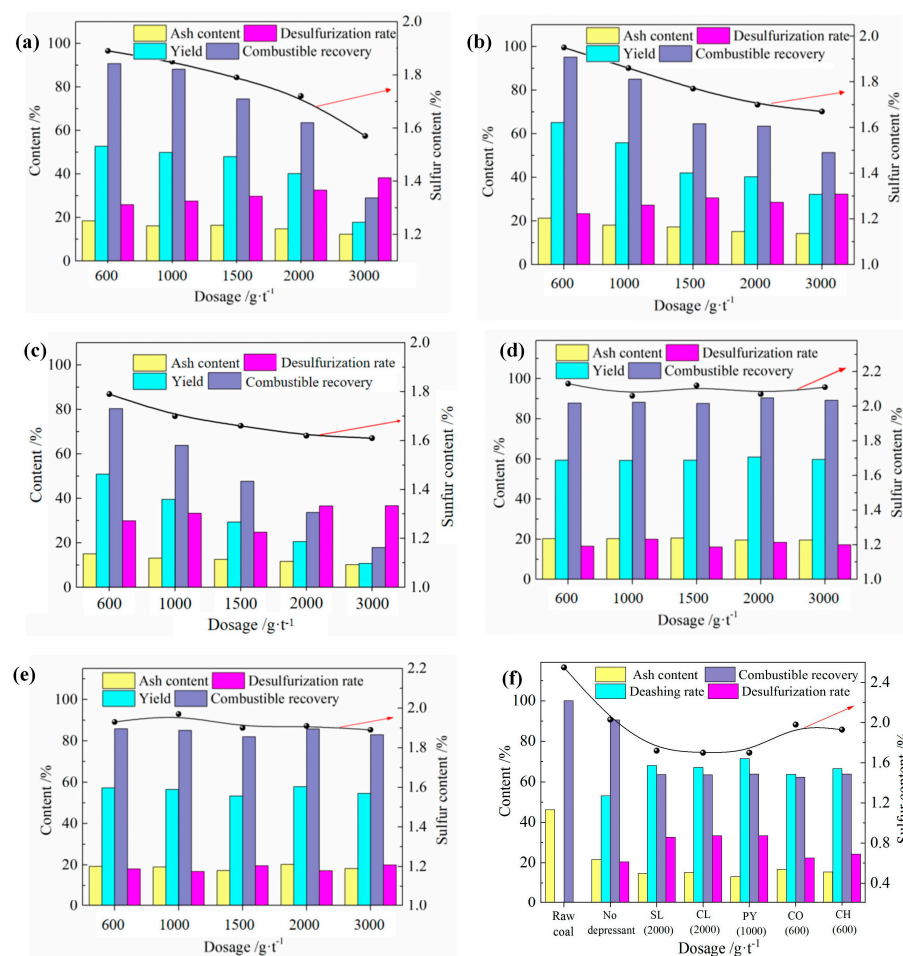


Figure 5. The average yield, sulfur content, ash content, desulfurization rate, and combustible recovery against various dosages: (a) SL, (b) CL, (c) PY, (d) CO, (e) CH, and (f) comparison of flotation results of each depressant.

Besides that, the dosage of organic depressants also showed a greater influence on combustible recovery. The combustible recovery was above 60% while the sulfur content was the lowest in clean coal for organic depressants as compared to inorganic depressants, as summarized in Figure 5f. Figure 5f shows that the combustible recovery for organic depressants (SL, CL, and PY) was 63.60%, 63.46% and 63.83%, respectively, while the sulfur contents of clean coal were 1.72%, 1.70%, and 1.70%, and the ash contents were 14.76%, 15.19%, and 13.16%, respectively. Here, the combustible recovery, desulfurization

rate, and deashing rate of PY were the highest, with the least dosage as compared to LS as the depressant. On the other hand, when compared without depressants, the sulfur content of clean coal did not decrease when inorganic depressants (CaO and $\text{Ca}(\text{ClO})_2$) were used, while the ash content of clean coal was also observed to be higher than that using organic depressants. These results showed that the desulfurization ability of organic depressants was better than that of inorganic depressants, albeit with the sacrifice of some of the combustibles. It is also noteworthy that the highest desulfurization rate was only 33.33%. The main reasons for the low desulfurization rate may be as follows: the embedded particle size of pyrite in coal was fine, and the coal-pyrite bodies proportion was high due to insufficient dissociation. Therefore, pyrite floated along with clean coal during flotation. In addition, the higher ash content reduced the percentage of sulfur in the raw coal sample.

3.3. The Adsorption Behaviors

3.3.1. The Adsorption Amount

The relationship between the adsorption amount of organic depressants on the coal-pyrite surface and depressant concentration is shown in Figure 6a. It can be seen that the adsorption amount was positively correlated with the initial concentration of depressants. The three depressants, PY, SL, and CL, were almost entirely adsorbed onto the pyrite surface when the initial concentration of depressants was low (10–20 mg/L). However, the adsorption amount of PY was higher than LS when the initial concentration of depressant was over 30 mg/L. When the depressant concentration was highest at 50 mg/L, the adsorption capacity of PY was the highest at 0.90 mg/L. These results showed that PY, SL, and CL could be adsorbed by pyrite, and the adsorption ability of PY was better than that of LS.

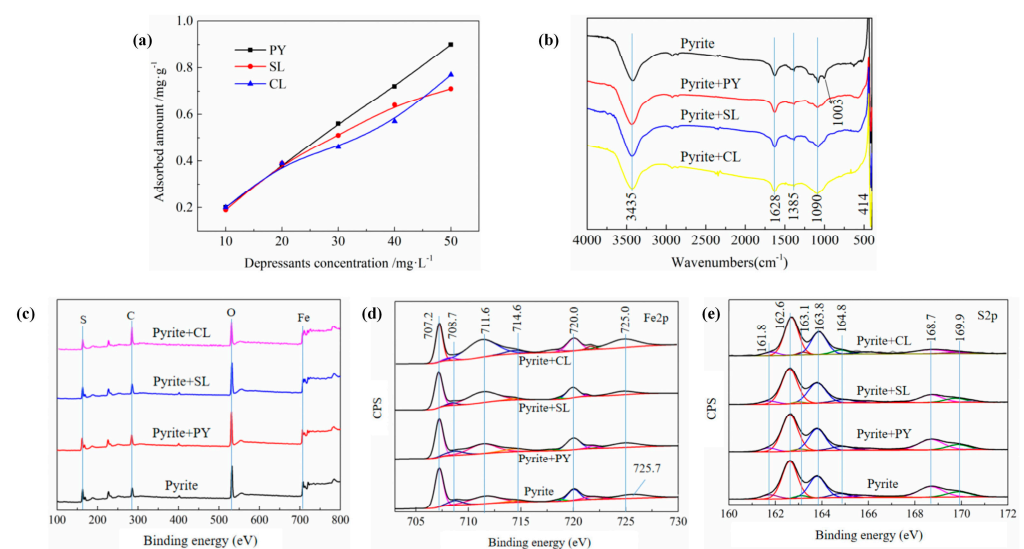


Figure 6. The adsorption behaviors of depressants on pyrite: (a) the adsorbed amounts, (b) the FTIR spectra, (c) the full-range XPS spectra, (d) Fe 2p, and (e) S 2p.

3.3.2. The FTIR Spectra of Pyrite in the Absence and Presence of Depressants

The FTIR spectra of the coal-pyrite surface before and after the addition of (organic) depressants (PY, SL, and CL) are shown in Figure 6b. In the infrared spectrum of coal-pyrite, 414 cm^{-1} , 1090 cm^{-1} , and 1385 cm^{-1} were the absorption peaks of pyrite. Among them, 414 cm^{-1} represented the stretching vibration peak of $\text{Fe}^{2+}\text{-}[\text{S}_2]^{2-}$, and 1090 cm^{-1} corresponded to the disulfide bond S-S [32]. The peak at 1003 cm^{-1} was the absorption peak of ferric sulfate. The peaks at 1628 cm^{-1} and 3435 cm^{-1} represented the stretching vibration of -OH [33]. The peaks near 2800 cm^{-1} and 2900 cm^{-1} represented the stretching vibration of C-H, which was due to the C-H bonds in coal-pyrite. The peak intensities at 1090 cm^{-1} and 1385 cm^{-1} were both weakened upon the addition of depressants, indicating

the adsorption of depressant onto the pyrite surface. There was a series of strong FeOOH absorption peaks at 400–800 cm^{-1} , and stretching vibration absorption peaks of sulfate ions in the wave number ranges of 1000–1300 cm^{-1} and 1300–1600 cm^{-1} . While no new absorption peaks were observed, the peak positions did not shift significantly upon the addition of depressants, indicating that there were no chemical interactions during the adsorption between pyrite and depressants [34,35].

3.3.3. Surface Chemical Group Analysis of Pyrite

The interaction between the organic depressants (PY, SL, and CL) and coal-pyrite was further analyzed via XPS. The full-range XPS spectra of pyrite in the absence and presence of these depressants are shown in Figure 6c. It was observed that the binding energies of surface species (Fe 2p, S 2p, and O 1s) did not shift from their original locations, implying that chemical adsorption of depressants on pyrite surface did not exist, as suggested earlier.

The Fe 2p and S 2p XPS spectra recorded from the surfaces of coal-pyrite with and without the addition of depressants are shown in Figure 6d,e. The Fe and S species were quantified based on the decoupling of the Fe 2p and S 2p spectra, respectively. The results are also summarized in Table 2. In the Fe 2p spectra, the binding energies at 707.2 eV and 720.0 eV corresponded to the spin orbitals of Fe(II)-S 2p_{3/2} and Fe(II)-S 2p_{1/2}, respectively, while the peaks at 708.7 eV, 711.6 eV, 714.6 eV, and 725.7 eV were attributed to FeO, Fe₂O₃, FeSO₄, and FeOOH, respectively [36]. In the S 2p spectra, two main peaks at 162.6 eV and 163.8 eV corresponded to the S 2p_{3/2} and S 2p_{1/2} orbitals of S₂²⁻, respectively. The lower binding energy at 161.7 eV and 163.4 eV was attributed to surface monosulfide S²⁻, the peaks at the higher binding energy (164.7 and 165.5 eV) were assigned to polysulfide or elemental sulfur S_n²⁻/S⁰, and the binding energies at 168.7 eV and 169.9 eV corresponded to SO₄²⁻ [37].

Table 2. The percentage of Fe and S species of pyrite in the absence and presence of depressant/%.

Species	Contents			
	Coal-Pyrite	Coal-Pyrite+PY	Coal-Pyrite+SL	Coal-Pyrite+CL
Fe(II)-S 2p _{3/2}	35.71	28.99	31.84	20.48
Fe(II)-S 2p _{1/2}	14.64	16.23	14.23	12.85
FeO	7.50	8.12	2.58	2.41
Fe ₂ O ₃	25.71	26.09	37.45	40.16
FeSO ₄	3.57	6.96	2.25	4.82
FeOOH	12.86	13.62	11.24	19.28
S ₂ ²⁻	61.82	59.85	62.35	69.46
S ²⁻	5.80	6.44	9.50	6.27
S _n ²⁻ /S ⁰	6.63	8.72	7.60	9.62
SO ₄ ²⁻	25.73	25.00	20.53	14.65

It can be observed from Table 2 that the Fe(II)-S 2p_{3/2} content on the pyrite surface decreased upon the addition of depressants, and the degree of reduction was observed to be the largest upon CL addition (from 35.71% to 20.48%). Moreover, the FeO content decreased from 7.50% to 2.58% and 2.41%, and the Fe₂O₃ content increased from 25.71% to 37.45% and 40.16% after adding SL and CL, respectively. This occurrence suggests that the oxidation of Fe(II)-S and FeO to Fe₂O₃ was promoted by SL and CL, which was conducive to the depression of pyrite due to the improved hydrophilicity of Fe₂O₃. It is worth noting that the content of hydrophobic S_n²⁻/S⁰ increased slightly upon the addition of depressants; however, the effect of S_n²⁻/S⁰ on the hydrophilicity of pyrite was negligible due to its lower concentration. The sulfate content, on the other hand, decreased upon depressants addition, possibly due to part of the sulfate being dissolved in the solution which then separated with the filtrate, which is also consistent with the FTIR test results.

3.4. MD Simulation Analyses

3.4.1. Quantum Chemical Properties of Depressants

The electrostatic potential (ESP) on the surfaces of PY and LS molecules are shown in Figure 7a,b (only the maximum and minimum values of each molecule are marked in the figure, whereby the cyan and yellow balls represent the minimum and maximum points of ESP, respectively). The ESP maximum point of the PY mainly appeared near the H atom. This is because the electronegativity of H is smaller than that of C and O atoms, and the H atom in the PY molecule was positively charged. Among them, the maximum point corresponding to H1 was 240.29 kJ/mol, followed by the maximum points corresponding to H2 and H3 (176.73 kJ/mol and 146.23 kJ/mol, respectively). The maximum values corresponding to H4 and H5 were 30.25 kJ/mol and 48.16 kJ/mol, respectively, which were significantly lower than the maximum values of H in the hydroxyl groups. This was due to the strong electron-withdrawing ability of oxygen atom which emphasizes the positive charge of H in the hydroxyl group. However, there was no maximum point near H6. This is due to the strong positive charge of the H atom in the hydroxyl group which leads to a large ESP near it, thus weakening the positive charge of H6. The minimum points of ESP were mainly concentrated near the O atoms of hydroxyl, in which one O atom corresponds to two minimum points, which are mainly contributed by the lone pair of electrons of the O atom. In addition, there is an ESP minimum point with molecular plane symmetry on each side of the benzene ring, which is caused by an abundant π electron cloud (negative contribution) to the ESP. It can be seen from the above analysis that the H atom in the hydroxyl group corresponds to the maximum point of surface electrostatic potential, which is prone to electrostatic interaction with the negatively charged center on the mineral surface, while the O atom in the hydroxyl group corresponds to the minimum point, which is prone to electrostatic interaction with the positive center of the mineral surface.

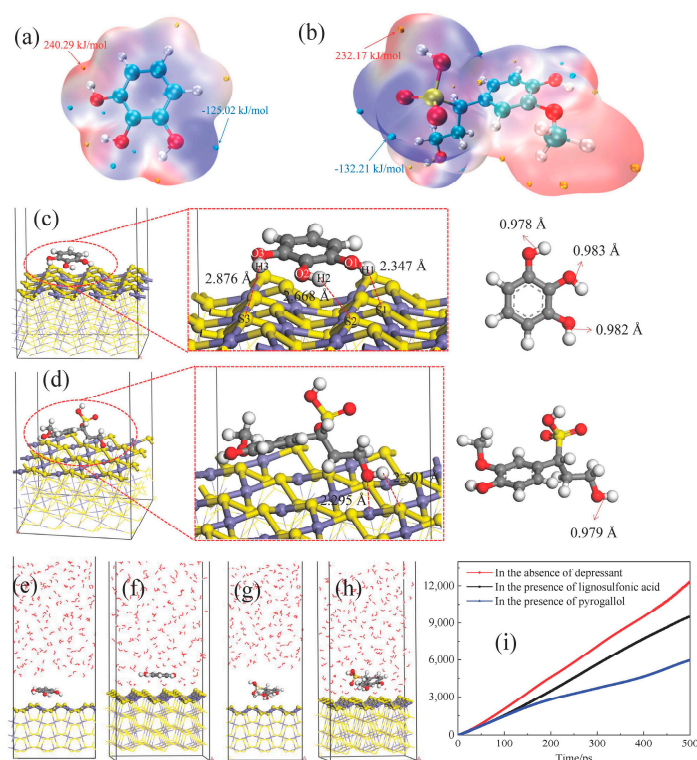


Figure 7. The molecular surface ESP of (a) PY and (b) LS; the equilibrium adsorption configuration of (c) PY and (d) LS; the initial adsorption configuration of (e) PY and (f) LS; the equilibrium adsorption configuration of (g) PY and (h) LS in the presence of water molecules; (i) MSD curves of water molecules in the absence and presence of depressant.

Furthermore, Figure 7b shows that the maximum point of ESP of LS appeared mostly near the H atoms, and the minimum point of ESP appeared near the O atoms. In the sulfo group, the maximum ESP value near the H atom was 232.17 kJ/mol, and the minimum ESP value near the double bond O atom was -132.21 kJ/mol. The maximum value of the ESP near the H atom in the alcohol hydroxyl group was 181.08 kJ/mol, and the minimum value of the ESP near the O atom was -128.95 kJ/mol, close to the maximum and minimum values. Therefore, both the sulfo group and the alcohol hydroxyl group of the LS molecule may be the electrostatic interaction sites.

3.4.2. Adsorption of Depressants on the Pyrite Surface

To further investigate the adsorption behavior of the depressant at the pyrite interface, MD simulations were conducted to calculate the interaction energy to quantitatively investigate the adsorption capacity of depressants on the surface of pyrite. The most stable adsorption configuration is shown in Figure 6c,d. The calculated adsorption energy results showed that the E_{ads} of PY and LS on the pyrite surface were -156.31 kJ/mol and -99.38 kJ/mol, respectively, indicating that the adsorption of PY was more favourable and thus stable compared to adsorption of lignosulfonic. In the pyrite/PY adsorption system, H-S bonds were formed between the H atoms of phenolic hydroxyl groups in the PY molecule and the S atoms of pyrite surface, in which the H1-S1, H2-S2, and H3-S3 bond lengths were 2.347 Å, 2.668 Å, and 2.876 Å, respectively. In addition, the bond lengths of O1-H1, O2-H2, and O3-H3 in PY increased from 0.971 Å, 0.975 Å, and 0.976 Å to 0.982 Å, 0.983 Å, and 0.978 Å, respectively. The largest change in bond length was for O1-H1, mainly because H1-S1 played a dominant role in the adsorption of pyrite and PY. In the pyrite/LS adsorption system, H-S and O-Fe bonds with bond lengths of 2.501 Å and 2.295 Å were formed between the H and O atoms of LS and the S and Fe atoms of pyrite. The OH bond length of LS was also observed to increase from 0.970 Å to 0.979 Å after adsorption.

The initial and stable adsorption configurations of depressant on pyrite surface in the presence of water molecules are shown in Figure 7e-h. The results showed that a stable water layer was formed on the pyrite surface after optimization of the pyrite/depressant/water system. This is consistent with the adsorption result of xanthate on pyrite surface simulated by Han et al. [38]. The distance between the O atoms of water molecules and the Fe atoms of pyrite was about 2.3 Å, which closely approximates the H-S bond length formed by PY with pyrite.

The D of water molecules was calculated according to Equation (5). The MSD curves of water molecules are shown in Figure 7i. The calculated D in the absence of depressant was 4.14×10^{-4} cm²/s, while the D in the presence of LS and PY was 3.34×10^{-4} cm²/s and 1.86×10^{-4} cm²/s, respectively. The reduced D in the presence of depressants indicated that the mobility of water molecules was hindered by depressants. It is worth mentioning that the D in the presence of PY was lower than that of LS, which indicated that PY had a better promotion effect on the hydrophilicity of pyrite than LS. This conclusion was in agreement with the former flotation results in Section 3.2.

3.4.3. The Effect of C Atom Doping on Hydrophilicity of Pyrite

The most stable substitution site of C atoms on the pyrite surface was calculated by Cao [39]. It was found that the replacement of C atoms in high site S atoms was more stable compared to Fe atoms and low site S atoms (Figure 8a). In this study, three C atoms were substituted for three high site S atoms to model the C-doped pyrite surface (Figure 8b). The calculation results showed that the adsorption energy of water molecules on the pyrite surface was 11.6 kJ/mol lower than that of the C atom-doped pyrite surface, signifying that the hydrophilicity of the pyrite surface was reduced due to the doping of C atoms. The stable adsorption configurations of water molecule on the pyrite and C-doped pyrite surfaces are shown in Figure 7c,d. It can be seen that the bond length between the O atom of water molecule and the Fe atom of FeS₂ was 2.12 Å, and the bond

length between the two H atoms of water molecule and the two S atoms of FeS₂ were 2.31 Å and 2.84 Å, respectively. A hydrogen bond formed easily between S and H atoms, however, with the replacement of S atoms by C atoms, and the adsorption sites of H on the pyrite surface decreased. Additionally, the adsorption capacity also reduced, resulting in a longer bond length between the atoms of water molecules and the atoms of the mineral surface.

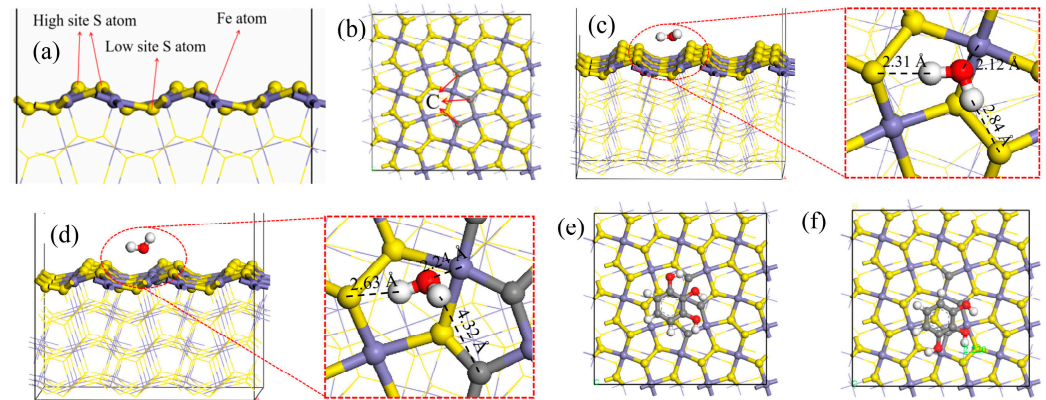


Figure 8. Stable configuration (a) pyrite surface, (b) C-doped pyrite surface; the stable adsorption configurations of water molecule on mineral surfaces: (c) FeS₂, (d) C-doped pyrite; the (e) initial and (f) stable configurations of PY adsorbed on the C-doped pyrite surface.

Besides affecting the adsorption of water molecule, the adsorption of depressants on the pyrite surface was observed to change due to the doping of C. The initial and stable configurations of PY adsorbed on the surface of C-doped pyrite are shown in Figure 7e,f. Here, it can be seen that the initial position of PY was near the C atom, and as the structure optimization progressed, PY moved towards the S atoms, forming hydrogen bonds between the hydroxyl H atoms and the S atoms of pyrite, while electrostatic adsorption occurred between the hydroxyl O atom of PY and the Fe atom of pyrite. As such, it is suggested that the doping of C atoms also occupies the adsorption sites of H atoms and is not conducive to the adsorption of PY.

3.4.4. The Effect of Depressants on Coal Flotation

Figure 9 shows the initial and stable configurations of the coal/water and the coal/PY/water systems. The calculated adsorption energy indicated that the E_{ads} without PY and with PY on the coal surface were -604.78 kJ/mol and -2444.13 kJ/mol, respectively. This indicates that when PY is present, the adsorption of water molecules on the coal surface is more stable, and inhibitors promote the adsorption of water molecules on the coal surface.

Figure 10a shows the concentration curve of water molecules on the coal surface before and after the addition of PY. It was observed that the concentration of water molecules on the coal surface increased after the addition of PY, and the inhibitor promoted the adsorption of water molecules on the coal surface. This is consistent with the results of the adsorption energy calculation. Figure 10b shows the MSD curves of water molecules on the coal surface before and after the addition of PY. Both water molecules and PY were observed to adsorb strongly on the coal surface. The MSD curves were linearly fitted, and the slope of the fitted lines was included into Equation (5) to calculate the diffusion coefficient D of water molecules on the coal surface. The results showed that before PY addition, the diffusion coefficient D of water molecules was 2.34×10^{-4} cm²/s, while the diffusion coefficient D of water molecules dropped to 2.24×10^{-4} cm²/s upon PY addition, indicating that the hydrophilicity of coal was improved slightly by PY, and was therefore not conducive to the flotation of coal. This again was consistent with the results of flotation experiments.

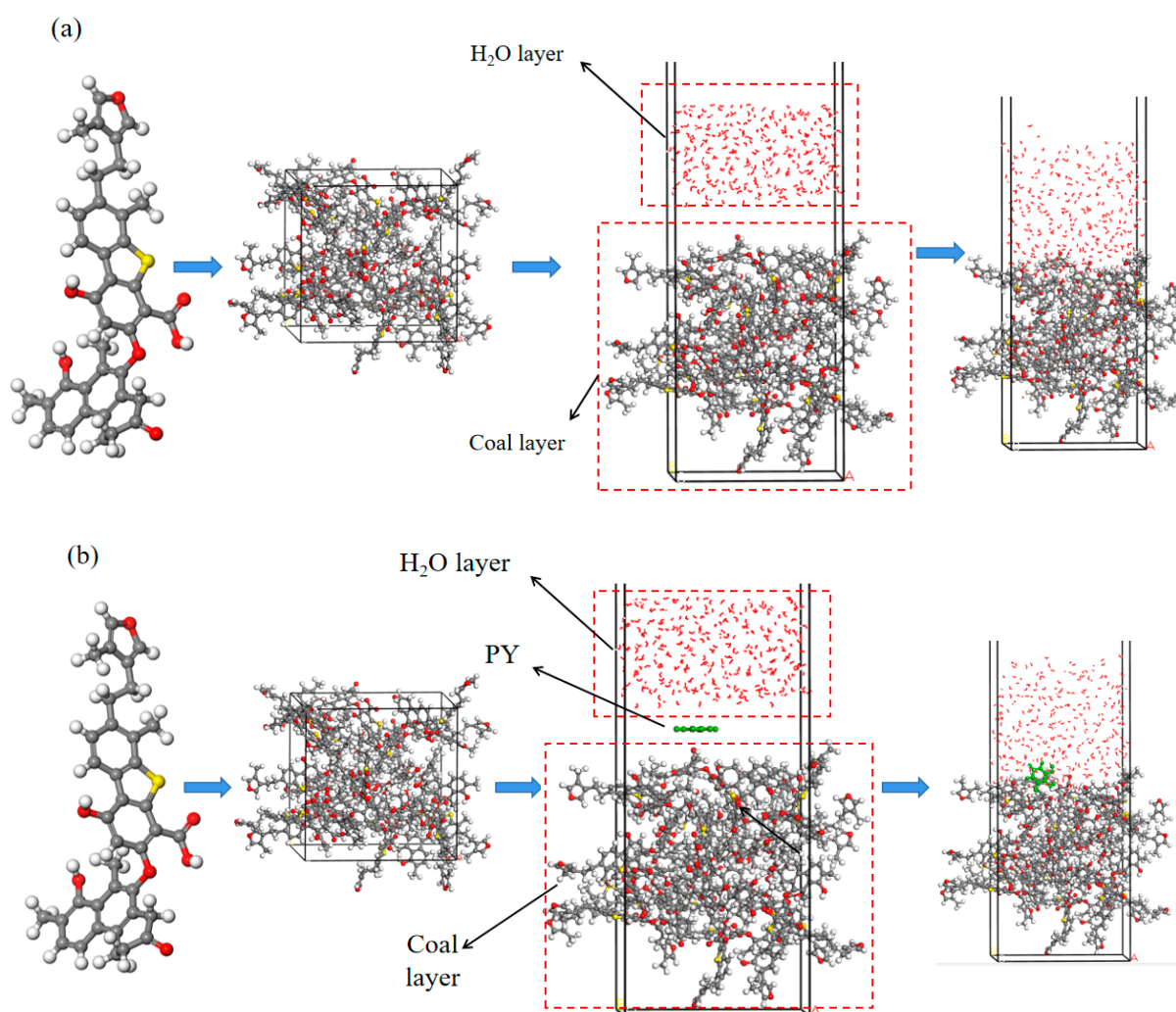


Figure 9. The initial and equilibrium configurations of (a) coal/water system and (b) coal/PY/water system.

In order to analyze the adsorption configuration of PY on the coal surface, the stable configuration of the coal/PY/water system was partially enlarged, as shown in Figure 10c. Figure 10c shows that PY was adsorbed on coal mainly through the hydroxyl groups. Among them, hydrogen bonds were formed between the hydroxyl H atoms of PY and the O atoms of the oxygen-containing functional groups on the coal surface, and between the hydroxyl O atoms of PY and the H atoms on the coal surface. Figure 10d shows the velocity of water molecules in the molecular dynamics process before and after PY adsorption. PY is adsorbed on coal through hydroxyl groups, which increase the residence time of water molecules on the coal surface, reduce the movement speed of water molecules, and slightly affect the hydrophilicity of coal, which is not conducive to coal flotation. This again was consistent with the results of flotation experiments.

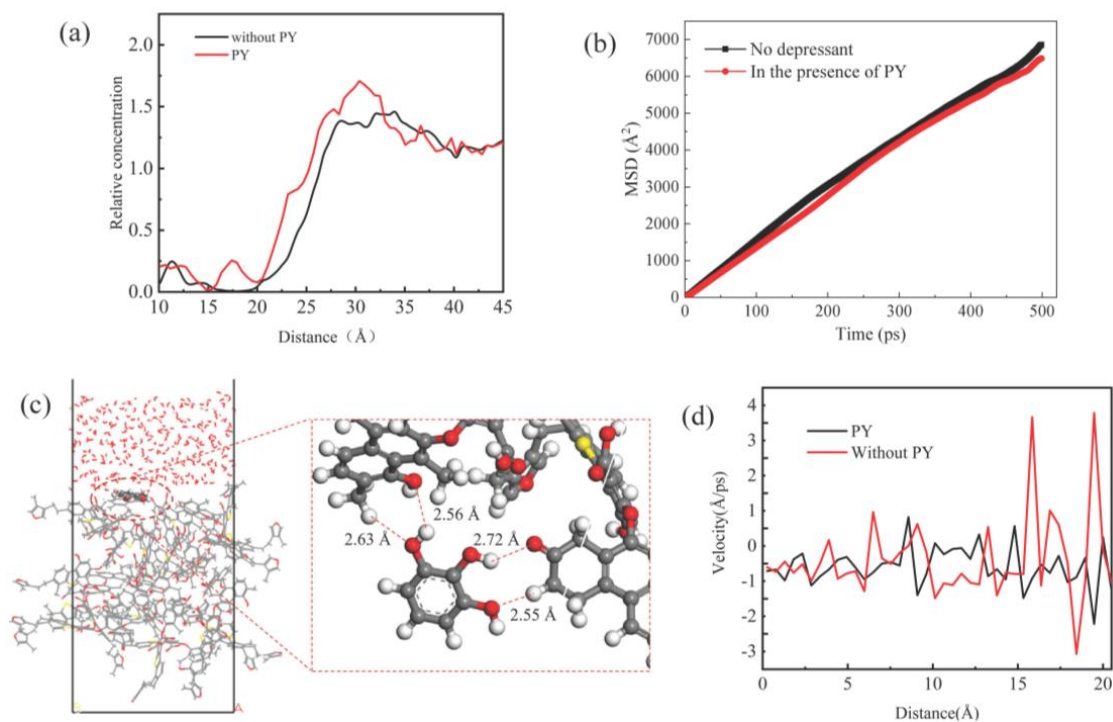


Figure 10. (a) Relative concentration of water molecules in the absence and presence of depressant, (b) MSD curves of water molecules in the absence and presence of depressant, (c) the microscopic adsorption configuration of PY on the surface of coal, (d) the velocity of water molecules in molecular dynamics processes.

4. Conclusions

The inhibition mechanisms of organic and inorganic depressants on coal-pyrite were studied. There was no significant difference among the desulfurization results using inorganic depressants and without depressants, indicating that the desulfurization performance of inorganic depressants was poor. When organic depressants were used, a combustible recovery of over 60% was achieved while the sulfur content of clean coal was reduced to 1.70%. Although PY had the advantage of less consumption (lower dosage) compared to SL and CL, part of clean coal was suppressed by organic depressants. In addition, the influence of Na^+ and Ca^{2+} on flotation results was not significant. The interaction form of SL, CL, and PY on pyrite was physical adsorption, whereby PY had a better adsorption capacity than SL and CL. The main reason for this is suggested to be that it contributed to the stronger adsorption capacity of PY on pyrite surface as compared to that of SL and CL, indicating that the adsorption of PY was more stable. The MSD results were consistent with the experimental results in which the adsorption of depressants was shown to improve the hydrophilicity of pyrite. Additionally, PY had a better effect on hydrophilicity than LS, which was again in agreement with the flotation results.

Author Contributions: G.C.: conceptualization, methodology, formal analysis, investigation, resources, writing—review and editing, supervision, project administration, funding acquisition. Y.L.: software, validation, formal analysis, investigation, data curation, writing—original draft. Y.C.: conceptualization, supervision. X.W.: supervision. E.L.: conceptualization, supervision. Y.G.: conceptualization, supervision. E.V.L.: writing—review and editing, supervision. All authors have read and agreed to the published version of the manuscript.

Funding: This research was funded by the “National Nature Science Foundation of China” (grant no. 22478231, U21A20321); “College Students’ Innovative Entrepreneurial Training Plan Program” (Grant No. 202310460076).

Data Availability Statement: Data are contained within the article.

Conflicts of Interest: The authors declare no conflicts of interest.

References

1. Yu, Y.X.; Liu, J.H.; Jia, X.F.; Min, C.; Liu, F.; Zhang, N.N.; Chen, S.J.; Zhu, Z.L.; Zhou, A.N. A new perspective on the understanding of high-Intensity conditioning: Incompatibility of conditions required for coarse and fine coal particles. *Miner. Process. Extr. Metall.* **2024**, *45*, 245–254. [CrossRef]
2. Matsobane, E.T.; Onifade, M.; Genc, B.; Bada, S. Comparative investigation of spontaneous combustion of biomass, hydrochar, coal and their blends using Wits-Ehac and thermogravimetric analysis. *Int. J. Coal Prep. Util.* **2024**. [CrossRef]
3. Resource Distribution and Development Trends of Major Coal-Producing Countries in the World. Available online: <https://futures.eastmoney.com/a/202108242060471076.html> (accessed on 20 September 2024).
4. World Energy & Climate Statistics- Yearbook 2024. Available online: <https://yearbook.enerdata.net/coal-lignite/coal-production-data.html> (accessed on 20 September 2024).
5. Cheng, G.; Zhang, M.N.; Zhang, Y.H.; Lin, B.; Zhan, H.J.; Zhang, H.J. A novel renewable collector from waste fried oil and its application in coal combustion residuals decarbonization. *Fuel* **2022**, *323*, 124388. [CrossRef]
6. Han, W.B.; Zhou, G.; Xing, M.Y.; Yang, Y.; Zhang, X.Y.; Miao, Y.N.; Wang, Y.M. Experimental investigation on physicochemical characteristics of coal treated with synthetic sodium salicylate–imidazole ionic liquids. *J. Mol. Liq.* **2021**, *327*, 114822. [CrossRef]
7. Tao, X.X.; Xu, N.; Xie, M.H.; Tang, L.F. Progress of the technique of coal microwave desulfurization. *Int. J. Coal Sci. Technol.* **2014**, *1*, 113–128. [CrossRef]
8. Xiong, M.J.; Huang, Y.T.; Fu, J.G.; Zhao, D.; Wang, X.B. Study on deashing, desulfurization and upgrading of high sulfur coal by deep-flotation combined with chemical oxidation. *Clean Coal Technol.* **2020**, *26*, 64–71.
9. Shen, Y.F.; Hu, Y.F.; Wang, M.J.; Bao, W.R.; Chang, L.P.; Xie, K.C. Speciation and thermal transformation of sulfur forms in high-sulfur coal and its utilization in coal-blending coking process: A review. *Chin. J. Chem. Eng.* **2021**, *35*, 70–82. [CrossRef]
10. Wang, S.W.; Xia, Q.; Xu, Q. Investigation of collector mixtures on the flotation dynamics of low-rank coal. *Fuel* **2022**, *327*, 125171. [CrossRef]
11. Zheng, K.H.; Zhang, W.J.; Li, Y.J.; Ping, A.; Wu, F.; Xie, G.Y.; Xia, W.C. Enhancing flotation removal of unburned carbon from fly ash by coal tar-based collector: Experiment and simulation. *Fuel* **2023**, *332*, 126023. [CrossRef]
12. Ahmad, W.; Salman, M.; Ahmad, I.; Yaseen, M. Process for desulfurization and demineralization of low rank coal using oxidation assisted froth floatation technique. *Chem. Eng. Res. Des.* **2024**, *205*, 301–311. [CrossRef]
13. Yang, X.L.; Albijanic, B.; Liu, G.Y.; Zhou, Y. Structure-activity relationship of Xanthates with different hydrophobic groups in the flotation of pyrite. *Miner. Eng.* **2018**, *125*, 155–164. [CrossRef]
14. Cheng, G.; Li, Y.L.; Cao, Y.J.; Zhang, Z.G. A novel method for the desulfurization of medium-high sulfur coking coal. *Fuel* **2023**, *335*, 126988. [CrossRef]
15. Wang, G.; Li, Y.Q.; Wang, E.M.; Huang, Q.M.; Wang, S.B.; Li, H.X. Experimental study on preparation of nanoparticle-surfactant nanofluids and their effects on coal surface wettability. *Int. J. Min. Sci. Technol.* **2022**, *32*, 387–397. [CrossRef]
16. Wang, C.Y.; Cen, X.W.; Xing, Y.W.; Zhang, C.H.; Li, J.H.; Gui, X.H. Depression mechanisms of sodium humate and 3-mercaptopropionic acid on pyrite in fine coal flotation. *Appl. Surf. Sci.* **2023**, *613*, 156151. [CrossRef]
17. Neisiani, A.A.; Saneie, R.; Mohammadzadeh, A.; Wonyen, D.G.; Chelgani, S.C. Polysaccharides- based pyrite depressants for green flotation separation: An overview. *Int. J. Min. Sci. Technol.* **2023**, *33*, 1229–12241. [CrossRef]
18. Jiao, F.; Li, W.; Wang, X.; Yang, C.R.; Zhang, Z.Q.; Fu, L.W.; Qin, W.Q. Application of EDTMPS as a novel calcite depressant in scheelite flotation. *Int. J. Min. Sci. Technol.* **2023**, *33*, 639–647. [CrossRef]
19. Zheng, Y.X.; Huang, Y.S.; Hu, P.J.; Qiu, X.H.; Lv, J.F.; Bao, L.Y. Flotation behaviors of chalcopyrite and galena using ferrate (VI) as a depressant. *Int. J. Min. Sci. Technol.* **2023**, *33*, 93–103. [CrossRef]
20. Li, Y.L.; Cheng, G.; Zhang, M.N.; Cao, Y.J.; Lau, E.V. Advances in depressants used for pyrite flotation separation from coal/minerals. *Int. J. Coal Sci. Technol.* **2022**, *9*, 54. [CrossRef]
21. Liu, S.; Wu, Y. Effects of Pyrite Depressor on High-Sulfur Coal Flotation. *Clean Coal Technol.* **2015**, *21*, 40–43.
22. Liu, D.Z.; Zhang, G.F.; Chen, Y.F.; Huang, G.H.; Gao, Y.W. Investigations on the utilization of konjac glucomannan in the flotation separation of chalcopyrite from pyrite. *Miner. Eng.* **2020**, *145*, 106098. [CrossRef]
23. Zhou, Y.; Albijanic, B.; Tadesse, B.; Wang, Y.L.; Yang, J.G.; Zhu, X.N. Flotation behavior of pyrite in sub-bituminous and meta-bituminous coals with starch depressant in a microflotation cell. *Fuel Process. Technol.* **2019**, *187*, 1–15. [CrossRef]
24. Qin, W.Q.; Hu, J.J.; Zhu, H.L.; Jiao, F.; Jia, W.H.; Han, J.W.; Chen, C. Effect of depressants on flotation separation of magnesite from dolomite and calcite. *Int. J. Min. Sci. Technol.* **2023**, *33*, 83–91. [CrossRef]
25. Cai, J.Z.; Deng, J.S.; Wang, L.; Hu, M.Z.; Xu, H.X.; Hou, X.A.; Wu, B.Z.; Li, S.M. Reagent types and action mechanisms in ilmenite flotation: A review. *Int. J. Miner. Met. Mater.* **2022**, *29*, 1656–1669. [CrossRef]
26. Chen, J.H.; Li, Y.Q.; Lan, L.H.; Guo, J. Interactions of xanthate with pyrite and galena surfaces in the presence and absence of oxygen. *J. Ind. Eng. Chem.* **2014**, *20*, 268–273. [CrossRef]
27. Zheng, X.F.; Pan, X.; Nie, Z.Y.; Yang, Y.; Liu, L.Z.; Yang, H.Y.; Xia, J.L. Combined DFT and XPS investigation of cysteine adsorption on the pyrite (100) surface. *Minerals* **2018**, *8*, 366. [CrossRef]
28. Xia, Y.C.; Yang, Z.L.; Zhang, R.; Xing, Y.W.; Gui, X.H. Enhancement of the surface hydrophobicity of low-rank coal by adsorbing DTAB: An experimental and molecular dynamics simulation study. *Fuel* **2019**, *239*, 145–152. [CrossRef]

29. Guo, J.Y.; Zhang, L.; Liu, S.Y.; Li, B. Effects of hydrophilic groups of nonionic surfactants on the wettability of lignite surface: Molecular dynamics simulation and experimental study. *Fuel* **2018**, *231*, 449–457. [[CrossRef](#)]
30. Khoso, S.A.; Hu, Y.H.; Lyu, F.; Liu, R.Q.; Sun, W. Selective separation of chalcopryrite from pyrite with a novel non-hazardous biodegradable depressant. *J. Clean. Prod.* **2019**, *232*, 888–897. [[CrossRef](#)]
31. Luo, Y.J.; Ou, L.M.; Chen, J.H.; Zhang, G.F.; Xia, Y.Q.; Zhu, B.H.; Zhou, H.Y. Mechanism insights into the hydrated Al ion adsorption on talc (001) basal surface: A DFT study. *Surf. Interfaces* **2022**, *30*, 101973. [[CrossRef](#)]
32. Li, W.Q.; Li, Y.B.; Wang, Z.H.; Yang, X.; Chen, W. Selective flotation of chalcopryrite from pyrite via seawater oxidation pretreatment. *Int. J. Min. Sci. Technol.* **2023**, *33*, 1289–1300. [[CrossRef](#)]
33. Wang, Z.; Liu, N.Y.; Zou, D. Interface adsorption mechanism of the improved flotation of fine pyrite by hydrophobic flocculation. *Sep. Purif. Technol.* **2021**, *275*, 119245. [[CrossRef](#)]
34. Zheng, K.; Li, H.P.; Xu, L.P.; Li, S.B.; Wang, L.Y.; Wen, X.Y.; Liu, Q.Y. The influence of humic acids on the weathering of pyrite: Electrochemical mechanism and environmental implications. *Environ. Pollut.* **2019**, *251*, 738–745. [[CrossRef](#)]
35. Zhao, K.L.; Wang, X.L.; Wang, Z.; Yan, W.; Zhou, X.; Xu, L.H.; Wang, C.Q. A novel depressant for selective flotation separation of pyrite and pyrophyllite. *Appl. Surf. Sci.* **2019**, *487*, 9–16. [[CrossRef](#)]
36. Cao, Z.; Chen, X.M.; Peng, Y.J. The role of sodium sulfide in the flotation of pyrite depressed in chalcopryrite flotation. *Miner. Eng.* **2018**, *119*, 93–98. [[CrossRef](#)]
37. Han, G.; Wen, S.M.; Wang, H.; Feng, Q.C. Interaction mechanism of tannic acid with pyrite surfaces and its response to flotation separation of chalcopryrite from pyrite in a low-alkaline medium. *J. Mater. Res. Technol.* **2018**, *9*, 4421–4430. [[CrossRef](#)]
38. Han, G.H.; Su, S.P.; Huang, Y.F.; Peng, W.J.; Cao, Y.J.; Liu, J.T. An insight into flotation chemistry of pyrite with isomeric xanthates: A combined experimental and computational study. *Minerals* **2018**, *8*, 166. [[CrossRef](#)]
39. Cao, Y.X.; Liu, W.L.; Xi, P.; Chen, J. Quantum chemistry investigation on influence of substituted carton concentration on the hydrophobicity of coal-pyrite surface. *J. Min. Sci. Technol.* **2018**, *3*, 186–193.

Disclaimer/Publisher’s Note: The statements, opinions and data contained in all publications are solely those of the individual author(s) and contributor(s) and not of MDPI and/or the editor(s). MDPI and/or the editor(s) disclaim responsibility for any injury to people or property resulting from any ideas, methods, instructions or products referred to in the content.